

# Phase-Dependent Catalytic Oxidation of Secondary Alcohols Using Spinel Cobaltite Catalysts Under Liquid- and Gas-Phase Flow Conditions

Alberto Tampieri,<sup>\*,[a]</sup> Federica Romanelli,<sup>[a, b]</sup> Michael Pittenauer,<sup>[a]</sup> Thomas Lederer,<sup>[a]</sup> and Karin Föttinger<sup>\*,[a]</sup>

Selective partial oxidation of alcohols is a straightforward synthetic pathway to access aldehydes and ketones, important building blocks for the chemical industry. The catalytic oxidation of higher secondary alcohols is challenging, which entails the need for low temperatures to preserve the selectivity or, in practice, the use of a liquid phase. In this work, we explored the applicability of Co-based spinel oxides as alternatives to noble metal-based supported catalysts for the oxidation of alcohols such as 2-butanol and 2-propanol. We developed a small-scale tri-phasic process in flow operable for consecutive weeks and using technical grade porous catalysts, en route to more

industrially-relevant systems, focusing on the practical aspects of the process.  $\text{Co}_3\text{O}_4$ ,  $\text{MnCo}_2\text{O}_4$ ,  $\text{NiCo}_2\text{O}_4$ ,  $\text{ZnCo}_2\text{O}_4$ , and  $\text{CoFe}_2\text{O}_4$  were synthesized by combustion and characterized by XRD, SEM, EDX, XPS,  $\text{N}_2$ -physisorption, and FT-IR spectroscopy. The same catalysts were tested in batch in the liquid phase to explore the impact of the reaction conditions on the reaction outcome and to rule out flow-specific effects. Gas phase reactions unveiled the different behavior of the same catalysts in different environments, highlighting phase-specific effects such as the beneficial (liquid phase) versus inhibiting (gas phase) impact of Mn doping.

## 1. Introduction

Selectively oxidizing a functional group and/or partially oxidizing a substrate, while preventing complete oxidation, requires highly selective catalysts with tailor-made properties.<sup>[1]</sup> Primary alcohols can be selectively oxidized to aldehydes, but over-oxidation can likely occur, leading to the formation of carboxylic acids; secondary alcohols can be oxidized to ketones, which are generally not further oxidized as ketone oxidation can only occur through C–C bond cleavage.<sup>[2]</sup> Oxidations of alcohols are traditionally carried out in anaerobic conditions using oxidizing stoichiometric reagents such as  $\text{CrO}_3$ ,  $\text{KMnO}_4$ ,  $\text{MnO}_2$ ,  $\text{SeO}_2$ , and  $\text{Br}_2$ ,<sup>[3]</sup> leading to both economic and environmental concerns. Hence, the imperative is to develop green, selective, and efficient aerobic catalysts for alcohol oxidation, utilizing molecular oxygen.<sup>[4]</sup> Several homogeneous catalysts have been developed

in the past decades based on transition metals;<sup>[5]</sup> on the other hand, heterogeneous catalysis offers important advantages over homogeneous processes in terms of product isolation, catalyst separation, and recycling, and it has a higher potential for the development of sustainable chemical processes.

The main application of alcohol oxidation in the industry is, by far, the oxidation of methanol to formaldehyde.<sup>[6]</sup> The Perstorp–Reichhold Formox process is an oxidative dehydrogenation over a mixed Fe and Mo oxide operating at relatively mild conditions ( $\sim 300\text{ }^\circ\text{C}$ ). The more widely used BASF process uses Ag and consists of two distinct steps: pure dehydrogenation followed by hydrogen combustion. As the first step is highly endothermic, it requires high temperatures ( $\sim 700\text{ }^\circ\text{C}$ ). Nevertheless, the BASF process is four times more popular than the oxide-based process, especially due to the relatively low productivity and selectivity of the latter. This clearly highlights the importance of researching novel active and selective heterogeneous catalysts. Moreover, achieving good selectivities with higher alcohols is more challenging.<sup>[7]</sup> This may require lower process temperatures and, in many cases, imply the need for a liquid phase. The presence of a solvent, which can interact with the reaction species, with the surface, and with the adsorbed intermediates, greatly increases the complexity of the system.<sup>[8]</sup> On top of that, in aerobic oxidation, the oxidant is a gas, resulting in an intricate triphasic system.

Aldehydes and ketones are important intermediates in the synthesis of pharmaceutically active agents, antioxidants, agrochemicals, and fine chemicals. 2-Butanone (methyl ethyl ketone, MEK) is typically used as a solvent, or it is employed for producing 2-ethyl hexanol, 2-ethyl hexanoic acid, and polyvinyl butyral, and for manufacturing plasticisers, rubber accelerators, and syn-

[a] Dr. A. Tampieri, F. Romanelli, M. Pittenauer, T. Lederer, Prof. K. Föttinger  
Institute of Materials Chemistry, Technische Universität Wien, Getreidemarkt  
9/165, Vienna 1060, Austria  
E-mail: [alberto.tampieri@tuwien.ac.at](mailto:alberto.tampieri@tuwien.ac.at)  
[karin.foettinger@tuwien.ac.at](mailto:karin.foettinger@tuwien.ac.at)

[b] F. Romanelli  
Department of Chemistry, Materials and Chemical Engineering, Politecnico  
di Milano, Piazza Leonardo da Vinci 32, Milan 20133, Italy

Supporting information for this article is available on the WWW under  
<https://doi.org/10.1002/cctc.202500778>

© 2025 The Author(s). ChemCatChem published by Wiley-VCH GmbH. This is an open access article under the terms of the [Creative Commons Attribution License](https://creativecommons.org/licenses/by/4.0/), which permits use, distribution and reproduction in any medium, provided the original work is properly cited.

thetic resins. The commercial production of MEK is typically based on the dehydrogenation of 2-butanol (2-BuOH) over Cu and Zn catalysts (occurring under harsh reaction conditions). However, the production of MEK through the oxidation of 2-BuOH is gaining interest because it offers the opportunity to work in mild conditions.<sup>[9]</sup> The oxidation of 2-BuOH to MEK has been studied on Pt/ $\gamma$ -Al<sub>2</sub>O<sub>3</sub><sup>[10]</sup> and Au nanoparticles.<sup>[11]</sup> Spinel-based systems have also been studied, including supported Mn<sub>3</sub>O<sub>4</sub>,<sup>[9]</sup> and MnCo<sub>2</sub>O<sub>4</sub> was tested as a catalyst for the selective oxidation of 1-butanol to butyraldehyde,<sup>[12]</sup> however, the process formed significant amounts of undesired acetaldehyde and propionaldehyde.

Recent studies of alcohol oxidation in the liquid phase tend to focus on supported nanoparticles or single-atom catalysts of metals such as Au, Ru, Pd, and Pt (Table S1),<sup>[13]</sup> which are highly active and selective with respect to their non-noble counterparts.<sup>[7]</sup> The rate-determining step (RDS) is widely acknowledged to be the activation of the C–H bond on the  $\alpha$ -carbon. The stability of supported metal catalysts is a critical drawback of such catalysts, especially in terms of sintering of nanoparticles and leaching due to the chelating effect of the reaction species. More resilient toward leaching is the class of oxide catalysts, which are bulk materials. On the other hand, the surface of such catalysts is generally ill-defined, presenting a challenge in identifying active sites and understanding reaction mechanisms. Nevertheless, the use of oxides allows great freedom in the modulation of the surface properties, e.g., by changing the distribution of cations and their oxidation states.

Among the oxides that are especially suitable as oxidation catalysts are the spinels AB<sub>2</sub>X<sub>4</sub>. A<sup>2+</sup> and B<sup>3+</sup> are metal cations, while X<sup>2-</sup> is an anion from the oxygen group.<sup>[14]</sup> The cubic spinel compounds belong to the space group Fd3m. In this structure, one-eighth of the tetrahedral and half of the octahedral interstices are occupied by cations.<sup>[15]</sup> Two extreme distributions of the cations are possible, albeit spinels with intermediate distributions are commonly observed: the normal distribution (A)[B<sub>2</sub>]X<sub>4</sub>, and the inverse distribution (B)[AB]X<sub>4</sub>, where the ions indicated by square brackets occupy octahedral sites, and the ions indicated by parentheses are located in tetrahedral sites.<sup>[15]</sup> An array of chemical and physical methods can be employed for the synthesis of spinels, spanning from solid-phase,<sup>[16]</sup> solution-state,<sup>[17]</sup> and vapor-phase methods.<sup>[18]</sup> Notably, spinel oxides with controllable composition, structure, valence, and morphology have emerged as effective catalysts in various chemical reactions, among which are NO<sub>x</sub> reduction,<sup>[19]</sup> CO oxidation,<sup>[20]</sup> CO<sub>2</sub> reduction,<sup>[21]</sup> hydrogen evolution reaction,<sup>[22]</sup> oxygen reduction reaction,<sup>[23]</sup> oxygen evolution reaction,<sup>[24]</sup> formaldehyde oxidation,<sup>[25]</sup> methane combustion,<sup>[26]</sup> urea oxidation.<sup>[27]</sup> Spinel containing earth-abundant transition metals have also been used as catalysts for partial alcohol oxidation in the liquid phase. High catalytic activity and selectivity were reported for the oxidation of benzyl alcohol over CuCo<sub>2</sub>O<sub>4</sub> and Cu<sub>0.25</sub>Mn<sub>2.75</sub>O<sub>4</sub>,<sup>[28]</sup> MnCo<sub>2</sub>O<sub>4</sub> and CoMn<sub>2</sub>O<sub>4</sub>, the latter being tetragonal, were also tested in the same reaction, with the Co-rich cubic spinel being the most active.<sup>[29]</sup> Co<sub>1+x</sub>Fe<sub>2-x</sub>O<sub>4</sub> spinel nanowires with different compositions were tested as catalysts for the oxidation of 2-propanol to acetone, both in the liquid and gas phase.<sup>[30]</sup> The

activity of the catalyst increased exponentially with increasing Co content. The catalytic activity was inhibited by the presence of Fe cations, which affect the electronic structure, and the active sites are constituted by ensembles of coordinatively unsaturated Co<sup>III</sup>. The presence of water in the liquid phase reaction is beneficial, whereas water vapour in the gas phase reaction lowers the reaction rate. Moreover, in the liquid phase, the catalyst shows substantially higher stability and reusability than in the gas phase.

In this study, we tested five Co-based spinels, Co<sub>3</sub>O<sub>4</sub>, MnCo<sub>2</sub>O<sub>4</sub>, NiCo<sub>2</sub>O<sub>4</sub>, ZnCo<sub>2</sub>O<sub>4</sub>, and CoFe<sub>2</sub>O<sub>4</sub>, in the partial oxidation of 2-butanol to MEK. In contrast to other studies focusing on the oxidation of 2-propanol in the gas phase with dopants in low quantities (Co:M = 16:1),<sup>[31]</sup> or in the liquid phase focusing on Co<sub>1+x</sub>Fe<sub>2-x</sub>O<sub>4</sub> and performing the reaction in batch,<sup>[30]</sup> we tested our stoichiometrically doped catalyst in the liquid phase in flow: the operation in flow is fundamental in order to assess the industrial feasibility of the catalytic process, as it allows better defining of the parameters for future scale-up.<sup>[32]</sup> Operation in flow allows following the evolution of the catalyst activity over time, which is important to evaluate the stability of the catalysts. This is precious information to aid the transition from homogeneous to heterogeneous oxidations of higher alcohols in the pharmaceutical and fine chemistry industry.<sup>[33]</sup> The catalysts were synthesized via the combustion method and characterized by XRD, SEM, EDX, XPS, N<sub>2</sub>-physisorption, and IR spectroscopy. Finally, we also performed reactions in batch for comparison, and in the gas phase to assess the impact of a liquid phase on the process, oxidizing 2-propanol to acetone.

## 2. Results

### 2.1. Synthesis, Phase Characterization, and Stability

The prepared cubic spinels share the same reflections, which are only slightly shifted according to the size of the unit cell (Figure 1a). The cell parameters obtained after Rietveld refinement are reported in Table 1, while the information provided about the spinel configuration has not been experimentally estimated, but refers to the configurations reported in the literature as the most stable ones for a composition. Spinel cobaltite is, in general, the most stable phase at low temperatures, which ensures stability during storage and enables low-temperature processing for its synthesis. Co<sub>3</sub>O<sub>4</sub>, which is a normal spinel,<sup>[34]</sup> has a broad range of stability in air, spanning from room temperature to about 900 °C,<sup>[35]</sup> above which it turns into a monoxide. The addition of Mn to the framework makes MnCo<sub>2</sub>O<sub>4</sub> an inverse spinel,<sup>[36]</sup> meaning that Mn significantly alters the distribution of cations. This also seems to influence the size of the unit cell, which is bigger for MnCo<sub>2</sub>O<sub>4</sub> than for Co<sub>3</sub>O<sub>4</sub>. As a result, it can be inferred that the M–O bonds would be longer. MnCo<sub>2</sub>O<sub>4</sub> behaves rather similarly to Co<sub>3</sub>O<sub>4</sub> upon heating, with the cubic spinel phase stable up to about 1000 °C.<sup>[37]</sup> The situation is different for NiCo<sub>2</sub>O<sub>4</sub>, which is also an inverse spinel.<sup>[36]</sup> Unlike Mn, which is much more versatile in terms of oxidation states, Ni<sup>2+</sup> is the only available state for Ni under these conditions; hence,

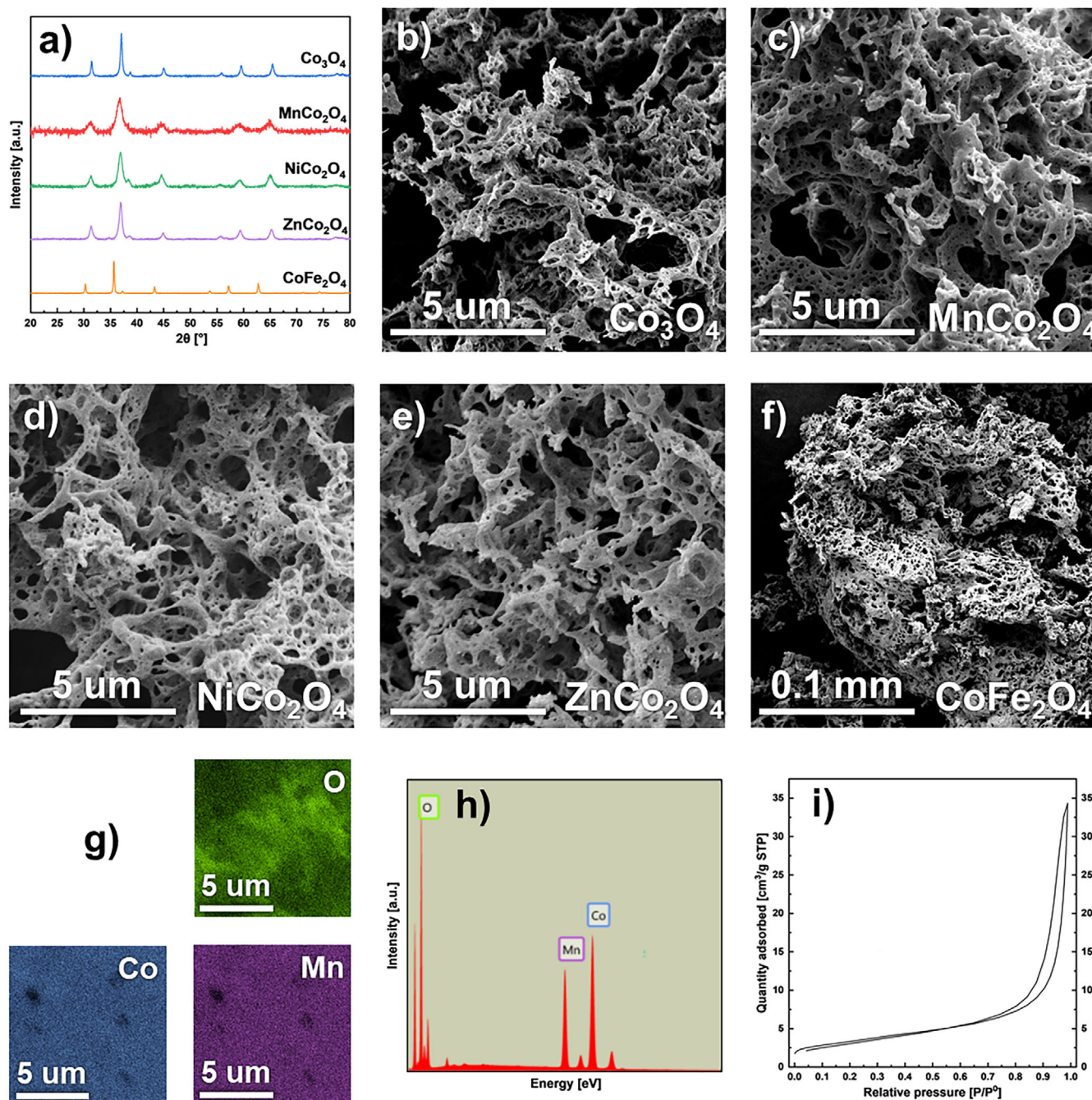


**Figure 1.** a) Powder X-ray diffraction patterns of the prepared catalysts; SEM micrographs of the synthesized b)  $\text{Co}_3\text{O}_4$ , c)  $\text{MnCo}_2\text{O}_4$ , d)  $\text{NiCo}_2\text{O}_4$ , e)  $\text{ZnCo}_2\text{O}_4$ , and f)  $\text{CoFe}_2\text{O}_4$ ; g) EDX maps of  $\text{MnCo}_2\text{O}_4$ ; h) EDX spectrum of  $\text{MnCo}_2\text{O}_4$ ; i)  $\text{N}_2$ -physorption profile of  $\text{Co}_3\text{O}_4$ .

all Co in the solid would be  $\text{Co}^{3+}$  as a result. The cell parameter and M–O bond lengths are also comparatively bigger. The presence of Ni also stabilizes the monoxide phase, which might form during the oxidation.<sup>[38]</sup> Similarly,  $\text{ZnCo}_2\text{O}_4$  also introduces  $\text{Zn}^{2+}$  only dopants, substituting all  $\text{Co}^{2+}$ , and stabilising the monoxide phase;<sup>[39]</sup> however,  $\text{ZnCo}_2\text{O}_4$  is a normal spinel.<sup>[40]</sup> The cell parameter of  $\text{ZnCo}_2\text{O}_4$  is more similar to that of  $\text{Co}_3\text{O}_4$ , highlighting a trend of the dependence of the cell sizes on the normal versus inverse distribution.  $\text{CoFe}_2\text{O}_4$  is different from the rest of the samples as it is a ferrite.  $\text{FeCo}_2\text{O}_4$  is not stable at room temperature: it disproportionates into two cubic spinels, a Co-rich

normal spinel like  $\text{Co}_3\text{O}_4$ , and an inverse one like  $\text{Fe}_3\text{O}_4$ .<sup>[41]</sup> On the other hand,  $\text{CoFe}_2\text{O}_4$ , which is also inverse, is stable over a very broad range of temperatures. Iron has a stronger preference for the  $\text{Fe}^{3+}$  oxidation state, whereas Co should be almost exclusively present as  $\text{Co}^{2+}$ .  $\text{CoFe}_2\text{O}_4$ 's diffraction pattern is strongly shifted toward lower angles, and the cell parameter is much higher than that of cobaltites.

The Rietveld refinement yielded the crystallite sizes of the materials. For most samples, the crystallite size remained almost unchanged during calcination. Only the crystallites of  $\text{NiCo}_2\text{O}_4$  (intense conversion of monoxide material into spinel)

**Table 1.** Expected structural features and parameters calculated by XRD of the prepared samples.

Entry	Sample	Expected oxidation states of the metal components	Expected configuration of the spinel structure	Expected position of $M^{2+}$	Cell parameter obtained from Rietveld refinement of XRD profiles (Å)	$M_{\text{tet}}\text{--O}$ bond length calculated from cell parameters (Å)	$M_{\text{oct}}\text{--O}$ bond length calculated from cell parameters (Å)
1	$\text{Co}_3\text{O}_4$	$\text{Co}^{2+}$ and $\text{Co}^{3+}$	Normal	Octahedral	8.084	1.981	1.981
2	$\text{MnCo}_2\text{O}_4$	$\text{Co}^{2/3+}$ and $\text{Mn}^{2/3+}$	Inverse	Tetrahedral	8.136	1.932	1.994
3	$\text{NiCo}_2\text{O}_4$	$\text{Ni}^{2+}$ and $\text{Co}^{3+}$	Inverse	Tetrahedral	8.121	1.828	1.990
4	$\text{ZnCo}_2\text{O}_4$	$\text{Zn}^{2+}$ and $\text{Co}^{3+}$	Normal	Octahedral	8.097	1.823	1.984
5	$\text{CoFe}_2\text{O}_4$	$\text{Co}^{2+}$ and $\text{Fe}^{3+}$	Inverse	Tetrahedral	8.377	1.886	2.053
Crystallite sizes obtained from Rietveld refinement of XRD profiles							
Entry	Sample	Before calcination (Å)	After calcination (Å)	After batch test (6 h) (Å)	After flow tests (7/10 d) (Å)	After flow test (20 d) (Å)	
6	$\text{Co}_3\text{O}_4$	253	242	251	310	340	
7	$\text{MnCo}_2\text{O}_4$	91	79	76	94	–	
8	$\text{NiCo}_2\text{O}_4$	26	101	103	109	–	
9	$\text{ZnCo}_2\text{O}_4$	160	161	150	176	–	
10	$\text{CoFe}_2\text{O}_4$	428	1133	–	–	–	

and  $\text{CoFe}_2\text{O}_4$  grew significantly; all materials but the latter are nanocrystalline ( $< 100$  nm). Finally, to assess the stability of the crystal structure under different reaction conditions, PXRD measurements were performed on catalysts after the catalytic tests (Section S5). While  $\text{Co}_3\text{O}_4$  and  $\text{MnCo}_2\text{O}_4$  are stable, for  $\text{ZnCo}_2\text{O}_4$  and  $\text{NiCo}_2\text{O}_4$ , the formation of monoxide phases was detected. The crystallite size of the catalysts did not change significantly during batch catalytic tests, while a more relevant growth was observed in flow conditions due to the much longer time of exposure of the catalyst to reaction conditions.

## 2.2. Characterization

Scanning electron micrographs of the prepared spinels show that these solids share the same porous morphology (Figure 1b–f). The formation of solids with such porous frameworks is a consequence of the selected synthesis method, forming a large amount of gases as bubbles and cavities, trapped in the final solid material. This is also the source of the very low apparent density of the catalysts. Looking at SEM images at 20,000x or 25,000x magnification, we could identify open macropores ranging from approximately 0.5 to 3  $\mu\text{m}$ . Analyzing the samples at 50,000x magnification, it was possible to detect secondary porosity due to cavities in the material with diameters below 0.05  $\mu\text{m}$ . Due to its magnetic properties,  $\text{CoFe}_2\text{O}_4$  could only be analyzed at a lower magnification.

$\text{N}_2$ -physisorption measurements were performed on cobaltite catalysts before, after 6-h batch catalytic tests in reference operating conditions, and after a flow catalytic test. The resulting adsorption and desorption isotherms have a shape similar to the one depicted in Figure 1i. The adsorption branch corresponds to a type II isotherm, typical for nonporous or macroporous adsorbents. This shape is the result of unrestricted monolayer-multilayer adsorption up to high values of  $P/P^0$ . The hysteresis loop is a type H3 loop, usually given by non-rigid aggregates of plate-like particles, but also if the pore network consists of macropores that are not entirely filled with pore condensate.<sup>[42]</sup> Comparing this information with the SEM images, it is clear that the hysteresis loop is given by the large cavities in the solids' structure. The specific surface area of each sample was calculated using the Brunauer–Emmett–Teller model (BET). The results are reported in Table 2. The specific surface of the solids directly obtained from the solution combustion step was about double, but it decreased during the calcination step. Nonetheless, the obtained values are comparable with those reported in the literature for spinel oxides synthesized via solution combustion.<sup>[43]</sup> The exposure to the reaction environment in the batch reactor caused a slight increase in the specific surface area of all tested catalysts. This behavior could be due to particle breakage caused by the stirring, which would make the internal porosity of the catalyst (observed by SEM) accessible to the gas, thus leading to an increase in the exposed surface. At any rate, the pore network does not seem to be altered by the batch process, as the shapes of the physisorption profile before and after reaction match (Figure S14a,b). Conversely, during the flow reaction, the catalyst powder is pelletized (Figure S31). With Zn, for exam-

**Table 2.** Results of the N<sub>2</sub>-physisorption, EDX, and XPS characterizations.

Entry	Sample	Surface area before reaction (m <sup>2</sup> /g)	Surface area after batch reaction (m <sup>2</sup> /g)	Co:M in the bulk obtained by EDX (atom:atom)	Co:M on the surface obtained by XPS (atom:atom)
1	Co <sub>3</sub> O <sub>4</sub>	13	15	–	–
2	MnCo <sub>2</sub> O <sub>4</sub>	20	22	2.00	0.77
3	NiCo <sub>2</sub> O <sub>4</sub>	7	13	2.04	1.16
4	ZnCo <sub>2</sub> O <sub>4</sub>	22	23	2.33	0.79
Entry	Sample	Surface area after flow reaction (pellet) (m <sup>2</sup> /g)		Surface area after flow reaction (ground pellet) (m <sup>2</sup> /g)	
5	ZnCo <sub>2</sub> O <sub>4</sub>	20		28	

ple, the surface area of the catalyst does not change significantly (Table 2, entry 5), whereas the isotherm profile of the pellet is significantly different as it presents a more pronounced hysteresis (Figure S14c). This change could be associated with a change in the pore structure from cylindrical and/or more regular pores in the starting material to ink-bottle-shaped pores in the pellet.<sup>[44]</sup> The pellet was ground and analyzed again (Figure S14d), and the physisorption profile obtained is more similar to the original one, with a comparable surface area.

Energy-dispersive X-ray spectroscopy was used to determine the bulk elemental composition of the cobaltite catalyst samples. In all analyzed catalysts, the metal ions appeared to be completely dispersed in the structure, and the composition of the catalysts is largely homogeneous throughout the samples. The corresponding EDX maps for O, Mn, and Co of MnCo<sub>2</sub>O<sub>4</sub> are reported in Figure 1g. Quantitative elemental analysis, performed by comparing the intensities of peaks corresponding to the different elements in the EDX spectra, showed that the ratio between the amount of Co and the amount of guest metal M (Mn, Ni, or Zn) in the bulk of the solid was close to the nominal value (Table 2). In ZnCo<sub>2</sub>O<sub>4</sub>, Co was slightly more abundant than expected.

X-ray photoelectron spectroscopy (XPS) measurements were performed to study the surface composition of Co<sub>3</sub>O<sub>4</sub>, MnCo<sub>2</sub>O<sub>4</sub>, NiCo<sub>2</sub>O<sub>4</sub>, and ZnCo<sub>2</sub>O<sub>4</sub> samples. The results concerning the quantification of elements on the catalyst surfaces are reported in Table 2. The observed distributions of metals differed substantially from those observed in the bulk through EDX measurements. For all analysed samples, the ratio between the amount of Co and the amount of guest metal M (Mn, Ni, or Zn) deviated from the nominal value of 2, and all surfaces were found to be depleted in Co. In MnCo<sub>2</sub>O<sub>4</sub> and ZnCo<sub>2</sub>O<sub>4</sub> the guest metals were even more abundant than Co. The spectrum of Co<sub>3</sub>O<sub>4</sub> includes the two spin-orbit split peaks (2p<sub>1/2</sub> and 2p<sub>3/2</sub>) associated with the 2p electron energy level of Co, and their satellites (Figure 2a). The presence and the abundance of different oxidation states of Co affect the shape of these peaks. Comparing the spectra of Co<sub>3</sub>O<sub>4</sub> before and after catalytic tests with other spectra reported in the literature,<sup>[45]</sup> it appears that both the divalent and the trivalent oxidation state of Co were present on the surface and that no substantial changes occurred during the reaction (Table S4). In line with our expectations, this suggests that the catalyst was not reduced to CoO or metallic Co, which could happen in case of an intense oxidation-via-dehydrogenation (but is unlikely

due to the highly oxidative environment), or hydroxylated to Co(OH)<sub>2</sub>, due to reaction with water. Importantly, no significant change in carbon content was observed (Table S3), implying that the recovered catalyst does not contain any carbon-based deactivating surface matter. Therefore, it can be inferred that the higher contribution of the water/organics component to the O 1s spectrum is due to the presence of adsorbed water (Figure 2b, and Table S4). The Co 2p spectra of all M<sub>x</sub>Co<sub>3-x</sub>O<sub>4</sub> materials match with previously reported data. The Co 2p spectrum of CoFe<sub>2</sub>O<sub>4</sub> is severely distorted by the presence of the underlying Fe LMM peak that hampers the fitting;<sup>[46]</sup> the spectra of MnCo<sub>2</sub>O<sub>4</sub> and NiCo<sub>2</sub>O<sub>4</sub> resemble that of Co<sub>3</sub>O<sub>4</sub>,<sup>[12,47]</sup> whereas the one of ZnCo<sub>2</sub>O<sub>4</sub> presents significantly more prominent satellite peaks.<sup>[48]</sup> The O 1s peak distribution of all fresh samples is similar to that of the Co<sub>3</sub>O<sub>4</sub> sample. The peak of MnCo<sub>2</sub>O<sub>4</sub> is considerably shifted toward higher binding energy. Finally, the M 2p spectra of the M<sub>x</sub>Co<sub>3-x</sub>O<sub>4</sub> materials also match the previously reported ones (Figure 2c).<sup>[12,46–48]</sup> In particular, Mn in MnCo<sub>2</sub>O<sub>4</sub> is present in multiple oxidation states (Table S4), including Mn<sup>4+</sup>, which is typically observed in this type of material.<sup>[18a,49]</sup> Mn<sup>3+</sup> is the main oxidation state present, followed by Mn<sup>4+</sup>. Mn<sup>2+</sup>, if any is present, is negligible. The presence of Mn in higher oxidation states at/near the surface is a main difference between the various cobaltite compounds.

Fourier transform infrared spectroscopy in attenuated total reflectance mode (FT-IR/ATR) was used to investigate metal-to-oxygen vibrations and to check for the presence of organic compounds on the catalyst surface after reaction. In all measured spectra, two intense bands associated with the OB<sub>3</sub> and ABO<sub>3</sub> vibrations of the spinel lattice (560 and 660 cm<sup>-1</sup> for Co<sub>3</sub>O<sub>4</sub>) were detected.<sup>[50]</sup> It is interesting to compare the position of these two peaks in the spectra of the spinels (Figure 3). The position of the peaks fits the trend of the normal/inverse configuration and the bond lengths. In general, the wavenumber of a vibrational mode is related to the strength of the bond and to the masses of the atoms involved: the stronger the bond (i.e., the larger the force constant associated with its vibration) and the smaller the reduced mass of the system, the larger the wavenumber. Since Mn has a lower atomic mass than Co, we would expect that MnCo<sub>2</sub>O<sub>4</sub> vibrates at slightly higher wavenumbers than Co<sub>3</sub>O<sub>4</sub>, the bond strengths being equal. However, the opposite happens, suggesting that the metal-to-oxygen bond might be weakened by the presence of Mn in the lattice, corroborating the XRD results. The infrared spectra resulting from

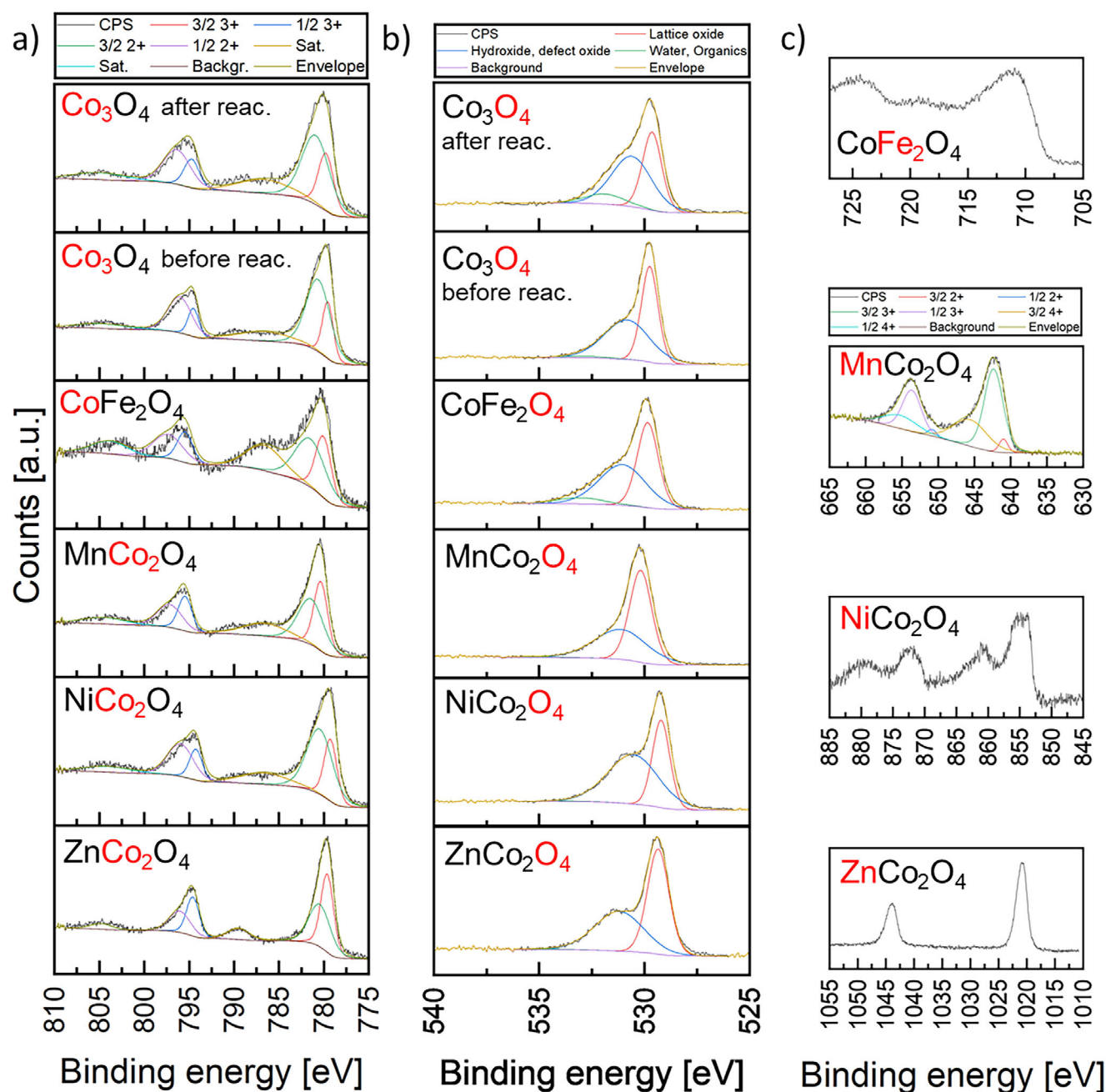


Figure 2. XPS spectra of a) Co 2p regions of the cobaltite samples, b) O 1s region, and c) metal M 2p region of the  $M_x\text{Co}_{3-x}\text{O}_4$  samples.

the analysis of the cobaltites before and after catalytic tests are shown in Section S8. No organic compounds seem to be retained by the examined catalysts after the washing. By focusing on the  $1000\text{--}4000\text{ cm}^{-1}$  region of the spectrum of  $\text{Co}_3\text{O}_4$  after the reaction, two additional peaks at  $1600$  and  $3300\text{ cm}^{-1}$  can be observed, corresponding to the bending and stretching modes of water, respectively.

### 2.3. Flow Liquid-Phase Testing

The conditions were initially optimized over a three-week period using  $\text{Co}_3\text{O}_4$  as a standard catalyst. This experiment aimed to

explore the effect of different operating conditions (liquid feed flow rate, pressure, and temperature) on the reaction outcome and to investigate the catalyst stability. The gas flow rate was kept constant, while different temperatures, pressures and liquid flow rates were selected within the operating conditions intervals reported in Table S5, while ensuring liquid phase conditions. The results of the optimisation test are presented in Figure 4. The experiment was initially carried out at 30 bar and  $200\text{ }^\circ\text{C}$ , feeding  $0.3\text{ mL/min}$  of liquid feed solution.  $\text{Co}_3\text{O}_4$  proved to be catalytically active in the oxidation of 2-butanol to MEK, with 6% conversion and 5% yield. Only 2-butanol and MEK were detected in the liquid-phase samples, whereas, in the gas phase, the only detected by-product was  $\text{CO}_2$ , presumably generated by further

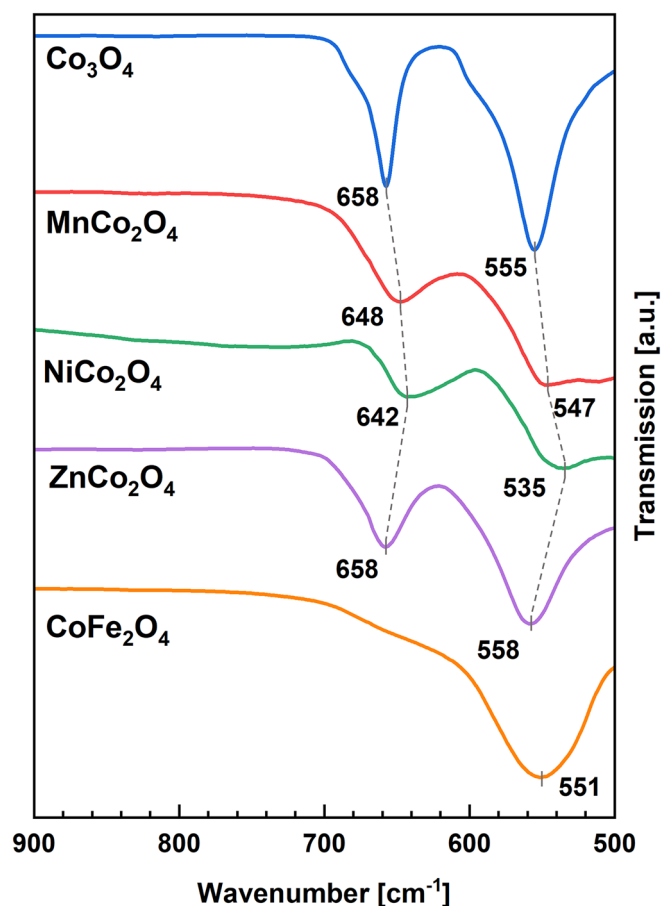


Figure 3. ATR-IR spectra of the prepared catalysts (M-O vibration range).

oxidation of MEK. Therefore, considering that no increase in the carbon content was observed by XPS, we assume that the gap to 100% selectivity corresponds to  $\text{CO}_2$ . After four days of operation in the same conditions, the liquid feed flow rate was lowered to 0.1 mL/min, leading to an increase of both the conversion (10%) and the yield (6%) as a result of the increase in the res-

idence time of the reacting mixture in the reactor. Then, the operating pressure was increased to 40 bar. This had the effect of increasing the oxygen concentration, and the conversion and yield increased even further (13% and 8%, respectively). After that, over a period of six days, the temperature was progressively increased to 215, 230, and 245 °C. Increasing the temperature above 200 °C did not enhance the yield of MEK, even though the conversion of 2-butanol increased at 245 °C (up to 17%). The concentration of  $\text{CO}_2$  in the gas-phase products increased, suggesting that, in these conditions, a larger fraction of MEK was further oxidized to  $\text{CO}_2$  and  $\text{H}_2\text{O}$ . Obviously, raising the temperature above 200 °C reduced the selectivity to the desired reaction product. Moreover, below 245 °C, the conversion does not significantly increase upon heating.

The expected increase in activity at higher temperatures seemed to be counterbalanced by a simultaneous deactivation of the catalyst, which might be due to a rearrangement in the oxide, including crystal growth, or by deposition of carbonaceous and/or organic matter. Indeed, when the temperature was lowered again down to 200 °C (days 15 and 16), a lower activity (6% conversion) was observed with respect to days 7 and 8, when the reactor had been operated under the same conditions. Finally, the temperature was further reduced to 185 and 160 °C. As expected, this led to a drop in the catalytic performance, both in terms of conversion (6% and 3%) and yield (3% and 1%). At 160 °C, almost no  $\text{CO}_2$  was detected in the gas phase. This suggests that, at lower temperatures, the catalyst is less active but more selective toward MEK. The chosen optimal conditions are a trade-off between catalyst activity and selectivity; 13% conversion and 8% yield were obtained on day 7, at 200 °C with 40 bar oxygen pressure and 0.1 mL/min liquid flow rate. These were selected as optimal operating conditions for comparing different catalyst compositions. A catalytic test was conducted using an aqueous solution of MEK as the feed for the oxidation with the flow reactor loaded with  $\text{Co}_3\text{O}_4$ . The purpose of this experiment was to examine the formation of compounds resulting from the successive oxidation of MEK. The analysis of reaction products

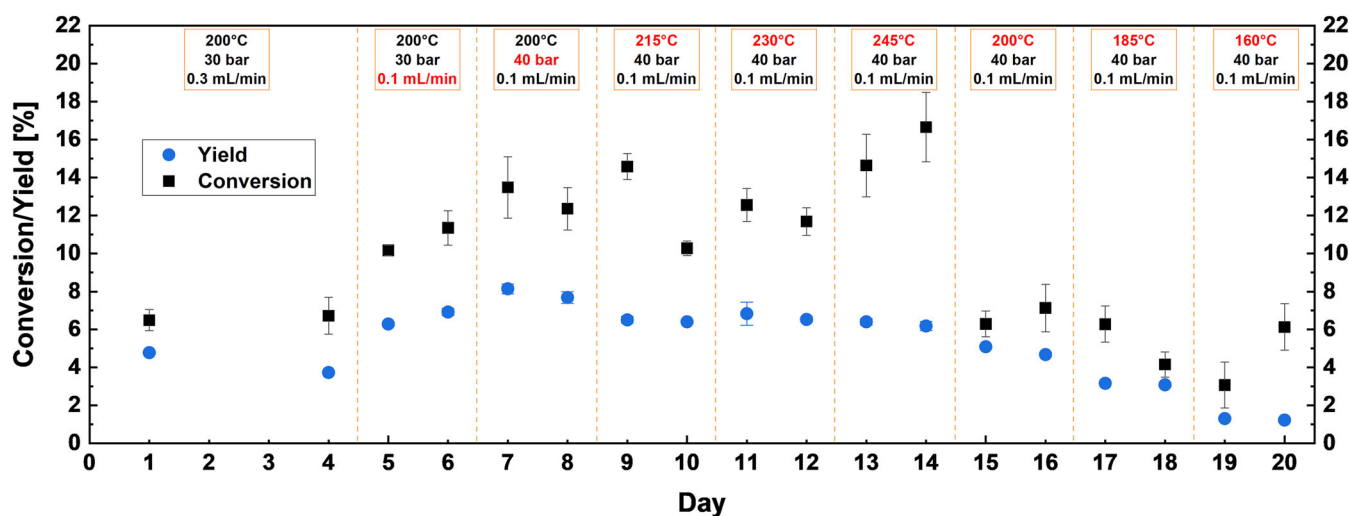
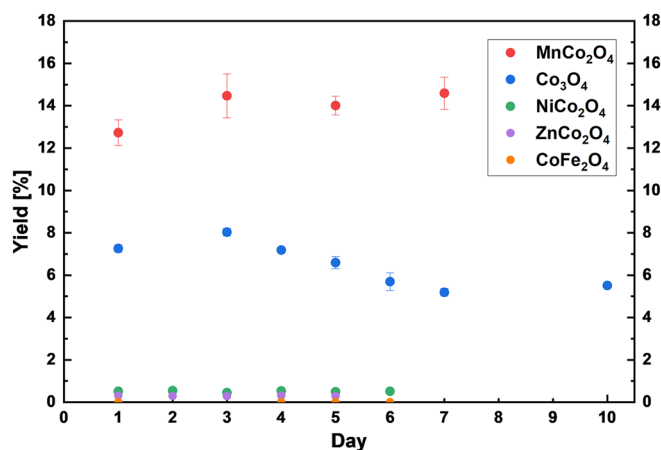


Figure 4. Conversions and yields of the liquid-phase catalytic oxidation of 2-butanol to MEK over  $\text{Co}_3\text{O}_4$  in a flow reaction: screening of reaction conditions; the parameters in red changed from the previous set of conditions.



**Figure 5.** Yields of the liquid-phase catalytic conversion of 2-butanol to MEK in flow reactions: screening of catalyst compositions. Conditions: 200 °C, 40 bar O<sub>2</sub>, 0.1 mL/min liquid flow rate.

was performed qualitatively, revealing only CO<sub>2</sub> as a detected product. Despite most of the MEK still being present at the reactor outlet, the production of CO<sub>2</sub> appeared significantly higher compared to the 2-butanol feed.

After selecting the optimal operating conditions, we investigated the activity of Co<sub>3</sub>O<sub>4</sub> and of the other Co-containing spinel oxides (CoFe<sub>2</sub>O<sub>4</sub>, ZnCo<sub>2</sub>O<sub>4</sub>, NiCo<sub>2</sub>O<sub>4</sub>, and MnCo<sub>2</sub>O<sub>4</sub>) (Tables S7 and S8). Figures S15–S19 illustrate the conversion of 2-butanol and the yield of MEK for each of them. Figure 5 compares the MEK yields obtained using the various catalysts. The activity of Co<sub>3</sub>O<sub>4</sub> slightly increased during the first days of operation, reaching a maximum of 8% yield after three days, but then decreased again from day 4 on, and reached a plateau of around 6% after a total of seven days of operation. The values of the conversion ranged between 9% and 16%. CoFe<sub>2</sub>O<sub>4</sub> was found to be inactive in the oxidation of 2-butanol: no MEK and CO<sub>2</sub> were formed, and no decrease in the concentration of 2-butanol was detected. When testing ZnCo<sub>2</sub>O<sub>4</sub> and NiCo<sub>2</sub>O<sub>4</sub>, minor amounts of MEK (corresponding to 0.3% and 0.5% yields, respectively) were detected in the liquid products for the entire duration of the catalytic tests. At the same time, a non-negligible decrease in the concentration of 2-butanol was observed, and CO<sub>2</sub> was detected in the gas phase. On the other hand, MnCo<sub>2</sub>O<sub>4</sub> proved to be the best among all tested catalysts, reaching up to 15% yield of MEK, and outclassing Co<sub>3</sub>O<sub>4</sub> by far. Comparing the conversion of 2-butanol and the concentration of CO<sub>2</sub> in the gas-phase with those observed for Co<sub>3</sub>O<sub>4</sub>, it appears that MnCo<sub>2</sub>O<sub>4</sub> is superior to Co<sub>3</sub>O<sub>4</sub> also in terms of selectivity to MEK. The catalytic performances of MnCo<sub>2</sub>O<sub>4</sub> proved to be stable during the seven days of catalytic testing.

## 2.4. Batch Liquid-Phase Testing

The oxidation process was also carried out in a laboratory batch reactor, equipped with an internal PTFE liner. Co<sub>3</sub>O<sub>4</sub> was selected as a reference to study the effect of different parameters (temperature, catalyst loading, catalyst composition, and pressure, conditions reported in Table S10) on the catalytic activity. The

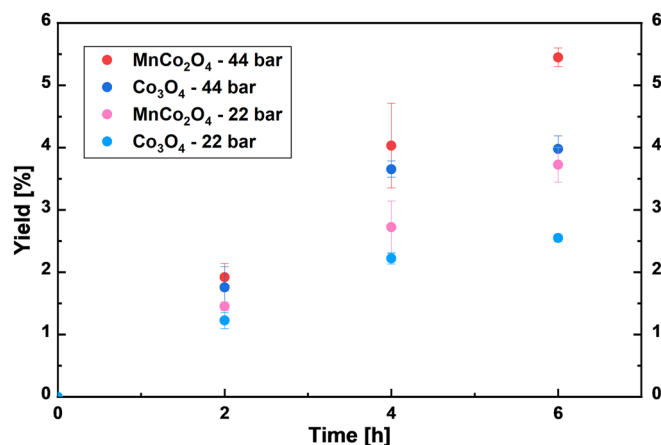


**Figure 6.** Yields of the liquid-phase catalytic conversion of 2-butanol to MEK in batch reactions: comparison of different operating pressures and catalysts. Temperature: 200 °C.

results are reported in Figures 6 (light blue), S20, and S27. For each catalyst and for each set of operating conditions, three catalytic tests with different contact times (2, 4, and 6 h) were performed. The effect of the reaction temperature on the catalytic activity was tested with Co<sub>3</sub>O<sub>4</sub> at 160 and 180 °C. In accordance with the results of the continuous flow catalytic tests, increasing the temperature led to an increase in the yield. The effect of the catalyst loading was investigated at 200 °C and 22 bar with 0.4 g of catalyst loading, half of the reference amount, leading to an almost proportional decrease in the yield.

The effect of different catalyst compositions on the catalytic activity was studied by testing the cobaltites ZnCo<sub>2</sub>O<sub>4</sub>, NiCo<sub>2</sub>O<sub>4</sub>, and MnCo<sub>2</sub>O<sub>4</sub> at 200 °C and 22 bar, with 0.8 g catalyst loading (reference conditions). Similarly to what we found in the continuous flow catalytic tests, ZnCo<sub>2</sub>O<sub>4</sub> and NiCo<sub>2</sub>O<sub>4</sub> were characterized by low catalytic activity and very low selectivity to MEK, whereas MnCo<sub>2</sub>O<sub>4</sub> was significantly more active than Co<sub>3</sub>O<sub>4</sub>. To study the effect of the pressure, a catalytic test was carried out at 200 °C and 44 bar with 0.8 g Co<sub>3</sub>O<sub>4</sub> and MnCo<sub>2</sub>O<sub>4</sub> (Figure 6). Like in the continuous flow catalytic tests, the increase in O<sub>2</sub> pressure led to a significant increase in the yield of MEK.

## 2.5. Gas-Phase Testing

The prepared Co<sub>3</sub>O<sub>4</sub> and MnCo<sub>2</sub>O<sub>4</sub> catalysts were also tested in the gas phase oxidation of 2-propanol to acetone (Figure 7). Over Co<sub>3</sub>O<sub>4</sub>, activity is detected from 70 °C on, with a local maximum in the activity at 195 °C. The concentration of the produced acetone plateaus from around 250 °C on, while the conversion increases until the maximum temperature of 400 °C. CO<sub>2</sub> is the main byproduct, and its concentration profile experiences a steep increase at 240 °C, after which it also reaches a plateau. Interestingly, the formation of hydrogen is also detected at higher temperatures. During cooling, the local maximum in the acetone formation was not observed. A second cycle was performed to assess the stability of the catalyst after the first cycle. The overall trend of the profiles appears to be similar, but the local activity maximum at 195 °C is not present, and the onset

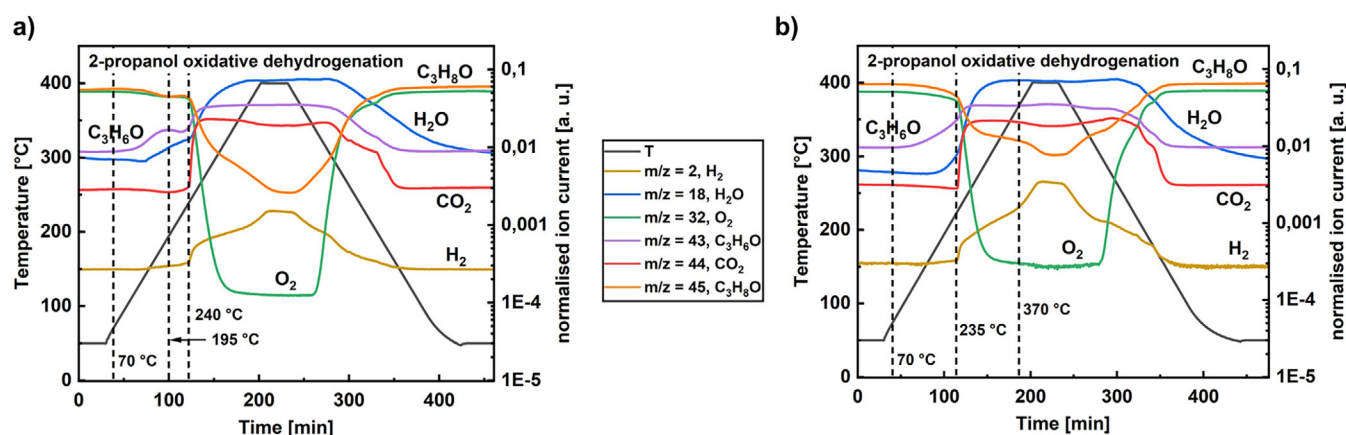


Figure 7. Concentration profile of species in the gas-phase catalytic oxidation of isopropanol to acetone over a)  $\text{Co}_3\text{O}_4$  and b)  $\text{MnCo}_2\text{O}_4$ : first temperature cycle.

of the reaction is shifted to higher temperatures. The plateau is shorter, although the maximum conversion is similar. The same test was performed on  $\text{MnCo}_2\text{O}_4$ . In this case, the activity onset is 70 °C, much like for  $\text{Co}_3\text{O}_4$ , and the  $\text{CO}_2$  formation starts at 235 °C, but the local maximum is much less pronounced. The profiles generally follow the same trend. While  $\text{MnCo}_2\text{O}_4$  was the most active catalyst in the liquid phase, its activity in the gas phase is lower. During the second cycle, the maximum conversion is considerably lower. For both solids, the spinel phase is converted into rock-salt, monoxide structures, indicating that the catalysts are reduced by the process (Figure S30).

Figure 8 contains the quantification data of the two reactions.  $\text{Co}_3\text{O}_4$  is slightly more active than  $\text{MnCo}_2\text{O}_4$  at all temperatures but 250 °C, at which the latter is considerably more active for both isopropanol and oxygen conversion. In the second cycle, the 2-propanol conversions are generally lower. Acetone is the only product until 200 °C, after which  $\text{CO}_2$  starts forming, reaching constant yields of around 5%. Above 200 °C, hydrogen also forms, and no plateau is seen in its production.

### 3. Discussion

Spinel oxide catalysts are active in the liquid-phase oxidation of 2-butanol to MEK. The batch tests at different loadings highlight the impact of the amount of catalyst on the rates. It is reasonable to assume that, in aqueous conditions, the reaction occurs according to the commonly accepted mechanism involving the dissociative adsorption of the alcohol on the catalyst surface, followed by its deprotonation. Both in continuous flow and batch catalytic tests, the catalyst activity was enhanced by pressure, i.e., by the concentration of the oxygen dissolved in the aqueous medium. Therefore, the reaction mechanism shall be one in which  $\text{O}_2$  could be involved in the rate-limiting step. One option is the Langmuir–Hinshelwood model, in which two surface species are bonded on neighboring sites (Figure 9). In our case, this entails the dissociative adsorption of  $\text{O}_2$  on the catalyst surface, followed by the extraction of hydrogen from the surface alkoxy intermediate, resulting in the production of a water molecule and a MEK molecule.

A second option is the Mars–van Krevelen mechanism, in which the hydrogen is extracted by the lattice oxygen contained in the spinel oxide structure, leaving a vacancy that is then filled by an oxygen atom coming from an  $\text{O}_2$  molecule. In this case, too, hydrogen extraction leads to the formation of  $\text{H}_2\text{O}$  and MEK. While no characterization result or catalytic test points toward one or the other, the Langmuir–Hinshelwood model is more typical of noble-metal catalysts, while the Mars–van Krevelen model is characteristic of oxide catalysts in gas-phase reactions, where lattice oxygen is available.

Our results show that cobaltite catalysts are relatively stable in the liquid phase and their activity is preserved over weeks of continuous operation, while previously it was only demonstrated by reusability in discontinuous settings. Nevertheless, during the initial exploratory flow test, the activity of  $\text{Co}_3\text{O}_4$  decreased over time when compared under the same conditions (days 7 and 8 versus 15 and 16, Figure 4). No deposited species were detected by FT-IR, nor was any chemical modification seen by XPS. The spinels are completely black, and colour changes cannot easily be perceived. Previously, it has been proposed that the presence of the aqueous phase is beneficial because it could dissolve inhibiting species into water,<sup>[30]</sup> even more so in a flow system. The catalyst does not seem to have undergone any considerable physical changes. The surface area did not decrease during the process, even though some crystallite growth was experienced (but stayed nanocrystalline, Table 1). A possible alternative explanation is that the system took time to reach the steady state, and that the catalyst bed underwent alteration during the process. The recovered solid turned from a powder, occupying the entire bed of the cartridge, to a pellet (Figure S31). The pressure and flow must have compressed the solid, probably facilitated by its sponginess and low apparent density. The structural collapse did not reduce the surface area, but decreased the volume of the empty space within the material, reducing the length of the bed (hence the contact time between the reaction species and the solid), and altering the mass transfer phenomena (via the change of pore structure to ink-bottle-shaped pores). The catalytic results of the test at constant conditions for  $\text{Co}_3\text{O}_4$  seem to corroborate this hypothesis, with the activity decreasing and then stabilizing (Figure 5), although conversions and yields for other catalysts

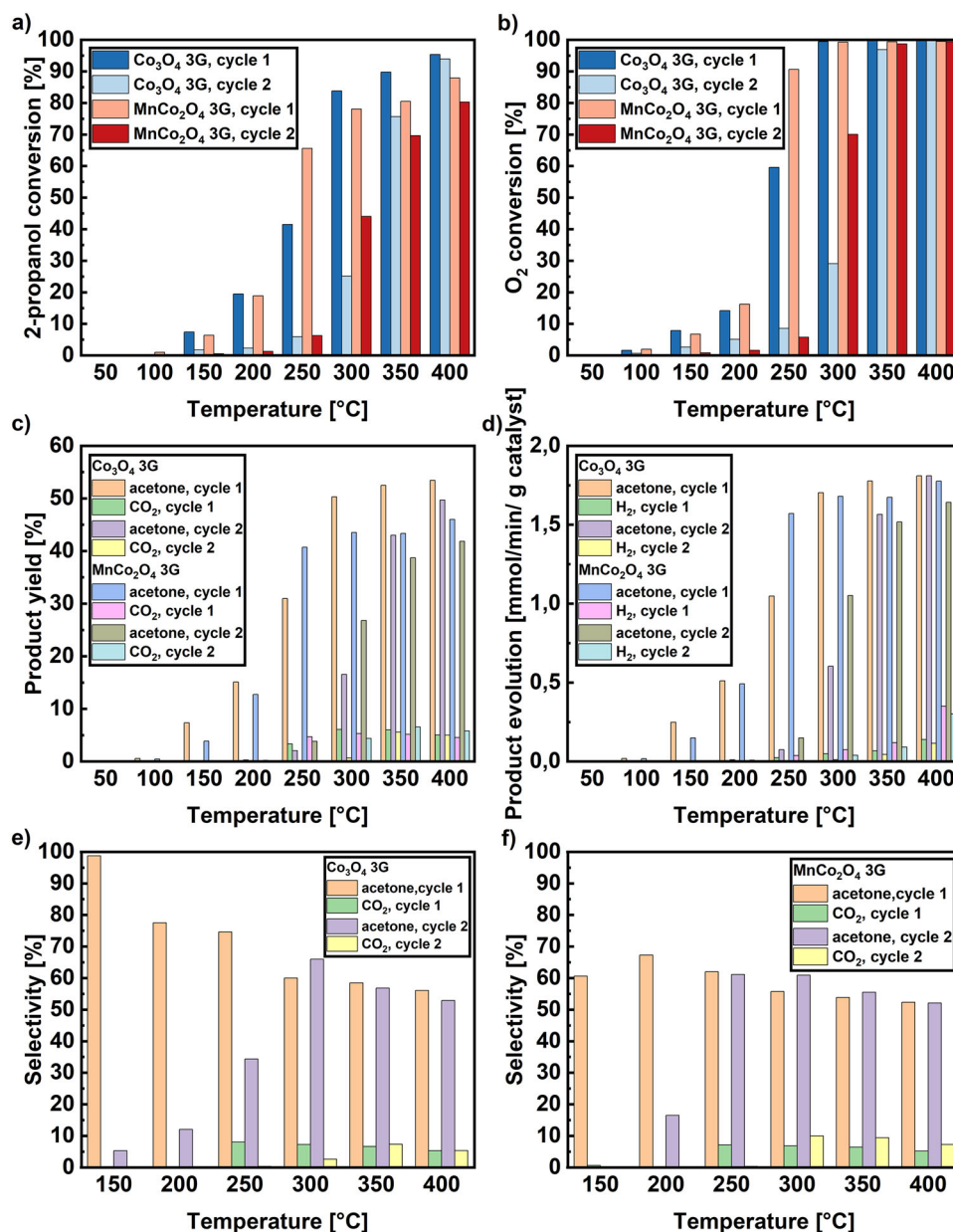


**Figure 8.** Quantitative overview of the gas-phase catalytic oxidation of isopropanol to acetone over  $\text{Co}_3\text{O}_4$  and  $\text{MnCo}_2\text{O}_4$ : a) isopropanol conversion; b)  $\text{O}_2$  conversion; c) acetone and  $\text{CO}_2$  yields; d) evolution of acetone and  $\text{H}_2$ . Selectivities of acetone and  $\text{CO}_2$  for e)  $\text{Co}_3\text{O}_4$  and f)  $\text{MnCo}_2\text{O}_4$ . Each figure includes, for each temperature, the values corresponding to  $\text{Co}_3\text{O}_4$  and  $\text{MnCo}_2\text{O}_4$  for both the first and the second consecutive temperature cycles on the increasing temperature ramp.

appear to be more stable over time (Section S9), even though they share the same spongy morphology and experience crystallite growth. Therefore, we cannot conclusively assign the partial deactivation of  $\text{Co}_3\text{O}_4$  in the test at constant conditions to neither a crystallite growth, nor a change in the surface area or pore network due to pelletization. The analysis of the ground pellet revealed that the pores did not undergo a major irreversible change, but instead, the new porosity was created by the particles compacted by the pressure. While other works focus on the use of nanoparticle catalysts in alcohol oxidation, with highly controlled shapes, precise compositions, and well-defined surfaces to make them more active and selective, the core of our

work is the development of a more industrially relevant flow process. Such catalysts might not be suitable for prolonged flow operation because their structure might be altered, and, on top of that, the flowing fluid phase would wash the particles away, requiring a special filter. Furthermore, the resulting bed would be densely packed, causing a high-pressure build-up, which would compress the bed, causing clogging. While we developed a working continuous flow system with our nanocrystalline combustion cobaltites in the form of micro/macroscopic porous powders, our study shows that particles with a relatively fragile and expanded framework, even though beneficial for the catalysis, might not be ideal candidates for such a pro-

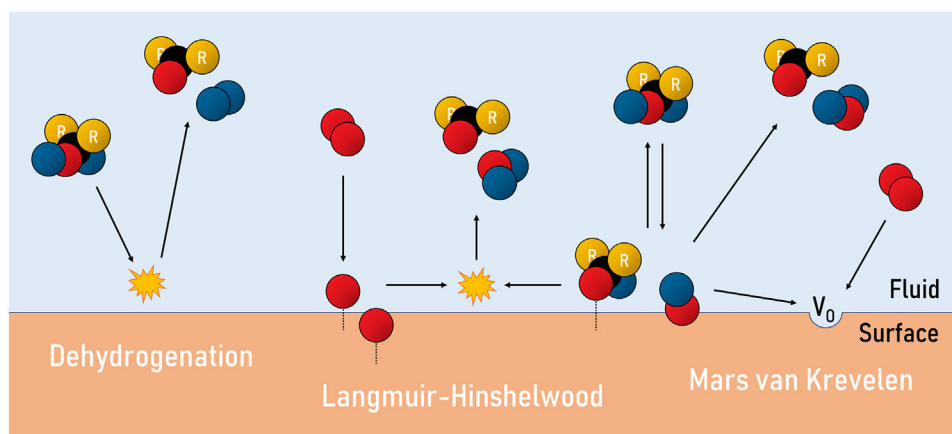
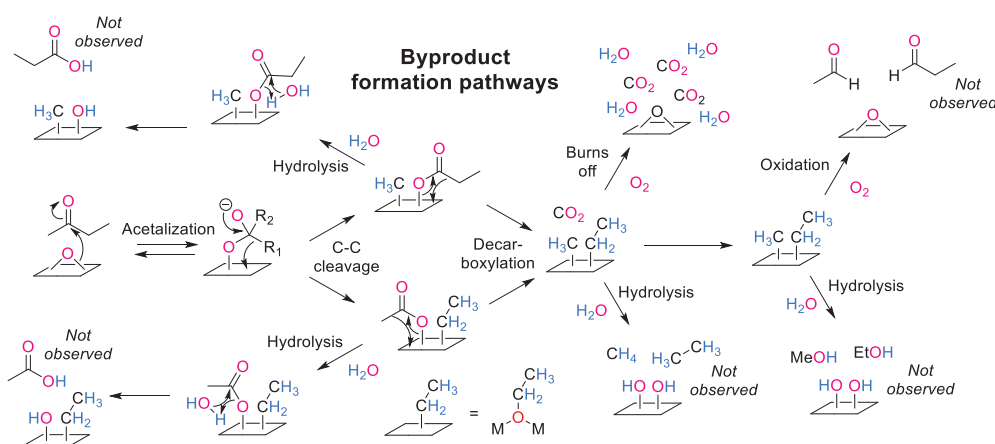


Figure 9. Possible alcohol oxidation mechanisms.



Scheme 1. Byproduct formation pathways.

cess. More sturdy and compact materials, such as those prepared by coprecipitation or thermal decomposition of salts, may be more suitable for industrial processes.

The selectivity to MEK was generally found to be below 100%. As shown by gas-phase GC analyses, CO<sub>2</sub> was detected as a reaction byproduct, suggesting that MEK might be consumed by consecutive oxidation to CO<sub>2</sub> and H<sub>2</sub>O, as confirmed by the mechanistic experiment of the MEK oxidation. Interestingly, no other byproducts were detected, neither in the liquid nor in the gas phase. A scheme of possible reaction mechanisms leading to byproduct formation through consecutive oxidation of MEK is reported in Scheme 1. MEK, as a ketone, may undergo acetalization-like reactions with oxygen-containing compounds such as water, an equilibrium reaction that favors the ketonic form. If acetalization occurs with lattice oxygen, additional decomposition events may follow. C–C cleavage could result in the formation of a carboxylate and an alkyl fragment, inducing further MEK oxidation. Carboxylates could undergo hydrolysis, releasing the corresponding acid (either propionic or acetic acid in this case), but no such compounds were observed in our mixtures.

This absence might be explained by the fact that carboxylate salt hydrolysis typically occurs in acidic conditions, and our medium is nonacidic. Consequently, the carboxylate may either

bind to the surface (although no related species were observed by FT-IR) or undergo decarboxylation. The remaining alkyl fragments, likely bound to lattice oxygens, may undergo various desorption pathways. They could hydrolyze into corresponding alcohols or, less likely, alkanes; they could be selectively oxidized to corresponding aldehydes; or they could simply combust to form carbon dioxide and water. Given the absence of any of the mentioned compounds except CO<sub>2</sub>, the latter scenario is proposed. The experiment using MEK as the only reaction species in the feed provides more insights into this process. Despite the fact that most MEK passed through the catalyst bed unreacted, the CO<sub>2</sub> production was significantly higher than with a 2-butanol solution feed. This suggests that CO<sub>2</sub> primarily originates from MEK, hinting to a consecutive oxidation rather than a breakdown of an intermediate, such as the alkoxide, in a 2-butanol oxidation scenario. While the formation of CO<sub>2</sub> lowers the selectivity by consuming the desired product, the absence of other organic compounds in the reaction products can also be interpreted as an advantage in terms of product separation. Concerning the effect of temperature, continuous flow catalytic tests using Co<sub>3</sub>O<sub>4</sub> showed that increasing the temperature enhances both the catalytic activity and the yield, while the selectivity toward MEK is higher at lower temperatures.

The screening of the catalyst composition showed that  $\text{MnCo}_2\text{O}_4$  was superior to all other catalysts both in terms of yield and selectivity; substituting Mn for Co also has the additional bonus of significantly decreasing the cost of the catalyst (Table S1, 27% decrease). Assuming that the migration of metal cations during the calcination step is fast enough and that the synthesized catalysts have a distribution of cations close to the thermodynamic one, some observations can be made. The improved performance of  $\text{MnCo}_2\text{O}_4$  might be attributed to its inverse spinel structure, in contrast to  $\text{Co}_3\text{O}_4$ , which has a normal spinel structure. In this view, Mn could have the effect of boosting the activity by pushing half of the  $\text{Co}^{3+}$  cations from octahedral to tetrahedral sites, positively influencing the  $\text{Co}^{3+}$  ensembles that have been previously proposed as active sites.<sup>[30]</sup> However,  $\text{NiCo}_2\text{O}_4$ , which is poorly active and selective, has an inverse spinel structure, too. Therefore, the inverted distribution alone cannot be the reason for the improved activity, even though it could be a contributing factor. The same applies to the longer M–O bonds in inverse configurations, which would entail more labile lattice oxygens, therefore more prone to reaction. Our results point to an enhancement connected to specific features of Mn, such as, for example, its large number of possible oxidation states. Interestingly, Mn was mostly present as  $\text{Mn}^{3+}$  and  $\text{Mn}^{4+}$ , according to XPS. The redox properties of Mn may be the key to its activity boost. The surface enrichment in Mn, as estimated by XPS, could have amplified this effect. Much like  $\text{NiCo}_2\text{O}_4$ , in  $\text{ZnCo}_2\text{O}_4$ , the guest metal can arguably be present only as a  $\text{Zn}^{2+}$  cation. This implies that Co is present only in the form of  $\text{Co}^{3+}$ , supposedly the active species; moreover,  $\text{ZnCo}_2\text{O}_4$  is a normal spinel, and it could be argued that  $\text{ZnCo}_2\text{O}_4$  is a direct analogue of  $\text{Co}_3\text{O}_4$ , whose  $\text{Co}^{2+}$  cations were substituted by  $\text{Zn}^{2+}$ . In this view, the catalytic results suggest that the low activity of  $\text{ZnCo}_2\text{O}_4$  is either due to an absence of a synergetic effect of  $\text{Co}^{2+}$ , or an inhibiting effect by  $\text{Zn}^{2+}$ , promoted by the enrichment in Zn on the surface. Conversely, Fe prefers the trivalent  $\text{Fe}^{3+}$  form; thus, all Co in  $\text{CoFe}_2\text{O}_4$  should be  $\text{Co}^{2+}$ .  $\text{CoFe}_2\text{O}_4$  was tested in flow conditions and proved to be completely inactive, implying that  $\text{Co}^{2+}$  alone does not take part in the catalysis;  $\text{Fe}^{3+}$  also inverts the spinel, increasing the M–O bond length, and might have an inhibiting effect as well. The effect of the addition of  $\text{Fe}^{3+}$  to  $\text{Co}_3\text{O}_4$  has been extensively studied in a previous work on 2-propanol oxidation over  $\text{Co}_{1+x}\text{Fe}_{2-x}\text{O}_4$ .<sup>[30]</sup> Even very small additions of  $\text{Fe}^{3+}$  in the framework of  $\text{Co}_3\text{O}_4$ , which was the most active composition, caused the activity to drop. Acetic acid was formed at higher temperatures, while we never detected any such byproduct; this effect could be the result of the different catalyst preparations or of the flow conditions.

Interestingly, while  $\text{MnCo}_2\text{O}_4$  is most active in the liquid phase at 200 °C, it is less active than the  $\text{Co}_3\text{O}_4$  in the gas phase. The enhanced Mn activity might be a liquid-phase effect related to the presence of a solvent, or attributed to the milder conditions. During the gas phase reaction, the catalysts were reduced to a monoxide, which is not the case for the liquid phase reaction. A main difference of the reaction in the liquid phase compared to the gas phase is the milder conditions, in particular the lower temperature, but also an excess of oxygen. These factors may help to keep the Mn in higher oxidation states and

enable its promotional effect, which may be lost when the catalyst gets reduced during the gas phase reaction. The higher activity of  $\text{MnCo}_2\text{O}_4$  compared to  $\text{Co}_3\text{O}_4$  is, however, seen at 250 °C in the gas phase reaction, which is also the point of highest selectivity toward acetone. The negative effect of Mn doping in the gas phase was also observed in another work.<sup>[31]</sup> The local maximum in activity for  $\text{Co}_3\text{O}_4$  observed at 195 °C is attributed to pure oxidative dehydrogenation, as acetone and water are the main products. However, even at 200 °C—the same temperature as the catalyst screening in the liquid phase—and even at a low oxygen conversion, an increase in hydrogen content is detected; the formation of hydrogen in other reports on similar systems is either not observed or not discussed. In aerobic oxidations proceeding via pure dehydrogenations, the alcohol is oxidized without the intervention of oxygen by forming molecular hydrogen, which is then combusted into water in a separate step. The net reactions, hence the observed products, are the same, but the mechanism would be completely different. We attribute the  $\text{H}_2$  formation setting in at around 240 °C for  $\text{Co}_3\text{O}_4$  and 235 °C for  $\text{MnCo}_2\text{O}_4$  mainly to alcohol dehydrogenation, and some contribution by total oxidation, which can be recognized by the  $\text{CO}_2$  rising simultaneously with  $\text{H}_2$ . Closer to the temperature maximum of 400 °C, significant contributions of dehydrogenation of 2-propanol can be seen. This points to reaction mechanisms in the gas and in the liquid phase which might be completely different. At higher temperatures, the total oxidation of 2-propanol is observed, which likely brings about the reduction of the spinel into a monoxide, as observed by XRD. As the selectivity profiles of the first and second consecutive cycles are in general very similar, except for some smaller shifts in temperature, we consider the catalyst reduction not to play a main role in determining the product distribution. The main difference concerns the absence of the low temperature maximum in acetone and water formation in the second cycle. This might be related to the consumption of certain oxygen species; however, this requires further investigation.

## 4. Conclusion

We developed an aerobic oxidation process for 2-butanol, our model substrate for a challenging secondary higher alcohol. This reaction has a higher industrial interest as it produces the important ketone MEK, compared to isopropanol oxidation to acetone, which is the standard model reaction in the field but is industrially less relevant. We studied the process using spinel cobaltites as catalysts, which are complex materials, and in the liquid phase, with all the additional complexity that having a solvent phase entails. The spinels contain earth-abundant and relatively low-cost elements and could serve as a viable alternative to noble-metal-based catalysts, commonly employed in the oxidations of higher alcohols. Our work aims to help bridge the gap from the previously reported processes using well-defined nanoparticulate spinels, to real conditions, using a more industrially relevant setup consisting of a liquid-phase flow reactor and technical grade catalysts, produced by a cheap, quick, and dirty combustion synthesis. The use of flow conditions rather

than batch ones, which is the most common setup in the literature for this system, allowed us to properly study the stability of the catalysts. Our active catalysts,  $\text{Co}_3\text{O}_4$  and  $\text{MnCo}_2\text{O}_4$ , are stable over long periods of time, albeit the macroporous structure collapsed into a pellet during the process. The prepared catalysts were stoichiometrically substituted cobaltites rather than doped, and this highlighted the impact of the presence of a metal in the framework, showing how the presence of Ni, Zn, and Fe is strikingly detrimental. Among the prepared samples,  $\text{MnCo}_2\text{O}_4$  stood out as it outperformed the standard  $\text{Co}_3\text{O}_4$  catalyst, and it is also cheaper in terms of starting materials. The boosted performance is attributed to Mn-specific effects, probably redox in nature, instead of an amplification of the activity of the  $\text{Co}_3\text{O}_4$  framework. The process favors the desired partial oxidation to MEK, but with considerable total oxidation to  $\text{CO}_2$ . No other byproducts are detected. We also performed the liquid-phase reactions in batch to test different conditions and rule out flow-specific effects, and in the gas phase, providing useful comparisons. Our catalysts behave differently in this last setting, with the Mn boosting effect turning into an inhibiting one, in line with previously reported data. The results highlight liquid phase-specific effects and the possibility that the reaction mechanism in the gas phase is completely different. On the same line, we experience the formation of hydrogen in the gas phase, which is often not experienced or reported in other works; this also provides interesting insights into alternative reaction pathways.

## 5. Experimental Section

### 5.1. Catalyst Synthesis

The spinel oxides were synthesized via the solution combustion method, starting from 50 mL aqueous solutions (deionized water, SIMPLICITY UV water purification system, Merck Millipore, 18.2 M $\Omega$ ·cm @ 25 °C) of metal nitrates ( $\text{Fe}(\text{NO}_3)_3 \cdot 9\text{H}_2\text{O}$  (for analysis, 99+%, ThermoScientific),  $\text{Co}(\text{NO}_3)_2 \cdot 6\text{H}_2\text{O}$  (reagent grade, 98%, Sigma-Aldrich),  $\text{Zn}(\text{NO}_3)_2 \cdot 4\text{H}_2\text{O}$  (for analysis,  $\geq 98.5\%$ , Merck),  $\text{Ni}(\text{NO}_3)_2 \cdot 6\text{H}_2\text{O}$  (for analysis,  $\geq 99\%$ , Merck), and  $\text{Mn}(\text{NO}_3)_2 \cdot 4\text{H}_2\text{O}$  (for analysis,  $\geq 98.5\%$ , Merck)) and using 3 equiv of glycine as a fuel (99%, Alfa Aesar). The mixture was poured into a beaker and heated until complete evaporation and combustion. The obtained solid was pulverized by grinding. All oxides but  $\text{CoFe}_2\text{O}_4$  were not single-phase spinels, and the specified oxidative thermal treatment was performed to achieve phase purity:  $\text{Co}_3\text{O}_4$  (300 °C, 2 h),  $\text{MnCo}_2\text{O}_4$  (300 °C, 2 h),  $\text{NiCo}_2\text{O}_4$  (450 °C, 4 h),  $\text{ZnCo}_2\text{O}_4$  (450 °C, 8 h).  $\text{CoFe}_2\text{O}_4$  also underwent a thermal treatment to remove residual carbon from the combustion from the surface and to anneal the material (450 °C, 8 h).

### 5.2. Catalyst Characterization

Powder X-ray diffraction (PXRD) patterns were measured on a PANalytical X'Pert powder diffractometer, operating in Bragg–Brentano geometry. The diffractometer was equipped with a Cu LFF X-ray tube operated at 45 kV and 40 mA (Cu  $K\alpha$ ), a BBHD mirror, a Malvern PANalytical MPD Pro (PW3050/60 goniometer) with 200 mm goniometer radius, and an X'Celerator semiconductor detector (RTMS "real-time multiple strip" technology). Measurements were performed for diffraction angles  $2\theta$  ranging from 20° to 80° with a

step size of 0.0201°. The samples were prepared according to the flat-specimen technique, using a flat Si single crystal wafer as a sample holder. PXRD patterns were interpreted using the program X'Pert HighScore Plus. The crystallite sizes and the cell parameters were calculated from diffraction patterns using Rietveld refinement. The XRD profiles of the samples after reaction are included in Section S5 for the liquid phase reactions and in Section S11 for the gas phase ones.

SEM and EDX analyses were performed using a FEI Quanta FEG 250 Scanning Electron Microscope, at 5 kV accelerating voltage and ~10 mm of working distance in high vacuum mode. The micrographs were taken on samples that were previously coated with Au:Pd 60:40 for 30 s with 30 mA using a Q150T S sputter coater (Quorum Technologies). The thickness of the deposited layer was about 8 nm. EDX measurements were performed in conjunction with SEM using an Octane Elite Super detector, with an acceleration voltage of 20 kV.

$\text{N}_2$ -physisorption measurements were performed to calculate the specific surface area of the samples from the respective adsorption isotherms by applying the Brunauer–Emmett–Teller (BET) theory. The measurements were performed using an ASAP2020 adsorption analyser (Micromeritics), after degassing the sample under vacuum (< 13  $\mu\text{bar}$ ) at 300 °C for 6 h. The surface area calculation (for  $0.5 < P/P^0 < 0.3$ ) was automatically performed using the program ASAP 2020 V4.00. The results of the analyses of  $\text{ZnCo}_2\text{O}_4$  are included in Section S6.

The XPS measurements were performed using a custom-built SPECS XPS spectrometer equipped with a monochromatized Al- $K\alpha$  X-ray source ( $\mu\text{Focus}$  350). The samples were loaded as a powder onto the sample holder using double-sided carbon tape. The binding energy of adventitious carbon (284.8 eV) was used for energy calibration. XPS data evaluation was carried out with CasaXPS software, employing Scofield sensitivity factors and the Shirley background type. The details of the quantification and the full quantification data are included in Section S7.

The FT-IR/ATR characterisations were performed using a Spectrum Two FT-IR Spectrometer (Perkin Elmer) equipped with a LiTaO<sub>3</sub> detector. Measurements were carried out using 16 scans at a 4  $\text{cm}^{-1}$  resolution between 400 and 4000  $\text{cm}^{-1}$  (MIR). For the measurement, the powder was pressed on the crystal with a metal cylinder. The full spectra before and after the reaction are included in Section S8.

### 5.3. Flow Liquid-Phase Catalytic Testing

Deionized water (Simplicity UV water purification system, Merck Millipore, 18.2 M $\Omega$ ·cm @ 25 °C), 2-butanol (99%, Sigma Aldrich), and oxygen (99.999% vol., Messer) were used as reagents to conduct liquid-phase catalytic tests in both flow and batch conditions. The testing was performed on a Phoenix Flow Reactor system (ThalesNano), comprising a gas module, a liquid–gas mixer, an HPLC pump (Azura P4.1S, Knauer), and a pressure module. The scheme and depiction of the system are shown in the Supporting Information (Figures S1–S3). The powder with a grain size > 65  $\mu\text{m}$  was packed in a tubular cartridge (CatCart, 70 mm, 0.76 mL, ThalesNano) and inserted into a stainless-steel cartridge holder inside the furnace of the reaction system. After the reactor set-up was assembled, the same start-up procedure was followed for each catalytic test. The system was pressurized under oxygen at the desired pressure and heated up to the desired temperature with a heating rate of 10 °C per min. A 1% vol. (0.11 M) aqueous solution of 2-butanol, previously degassed in an ultrasonic bath for 30 s, was then flown at the desired flow rate. The liquid phase was collected discontinuously in an ice-cooled, custom-made glass cold trap and was analysed with an offline GC-FID, while the uncondensed gases exited from the top

of the cold trap and were analyzed by an online GC-FID/TCD. The details of the GC analyses are described in Section 5.3. At the end of each catalytic test, the 2-butanol solution feed was stopped, and deionized distilled water was fed to the reactor for a few hours. Then, the liquid feed was stopped again, keeping only the gaseous oxygen feed for another few hours. The furnace was turned off and, once it had reached ambient temperature, the system was depressurized. After that, the gas feed was stopped, and the reactor was disconnected from the system and put inside an oven at 120 °C for overnight drying.

#### 5.4. Batch Liquid-Phase Catalytic Testing

The batch reactor set-up was composed of a PTFE gasketed autoclave reactor with an internal thermocouple and a PTFE liner (300 mL Series 4760 Pressure Vessel, Parr Instrument Company), a self-manufactured internal PTFE cap, a magnetic stirrer with heating plate (C-MAG HS 7 digital, IKA), an external thermocouple and a custom-made external aluminium heating jacket. The catalyst powder (0.4 g or 0.8 g) was weighed directly inside the PTFE liner. A magnetic stir bar was put inside the liner. 100 mL of 2-butanol solution was poured into the PTFE liner, which was put inside the lower part of the stainless-steel reactor. The PTFE cap was mounted on the upper part of the reactor, which was then closed and sealed. The reactor was pressurized with oxygen up to the selected initial pressure (corresponding to a higher pressure once the reactor was heated). The autoclave was positioned in the aluminium block on the heating plate, and the heating and magnetic stirring (500 rpm) were turned on. The heating was regulated from the heating plate. As the reactor temperature increased, the pressure increased, too. The time zero was defined as the point at which the system reached an internal temperature of 20 °C lower than the desired reaction temperature (due to the long time required to reach the desired temperature). After the desired time, the heating and the magnetic stirring were turned off, and the reactor was removed from the aluminium jacket. The reactor was cooled down until it reached ambient temperature. Then, it was slowly depressurized and opened. All the liquid droplets were collected from the walls of the upper and lower parts of the reactor, from the liner walls, and from the liner cap using a glass pipette, and they were mixed with the slurry remaining in the liner. To separate the liquid from the solid, the slurry was transferred to a vial and centrifuged at 4500 rpm for 12 min in a 2–16P centrifuge (Sartorius). The clarified solution was finally filtered in a syringe filter (0.2 µm pore size CHROMAFIL Xtra PTFE-20/25, Macherey-Nagel). The solid remaining at the bottom of the vial was washed with deionized distilled water and filtered using a paper filter (4–12 µm pore size DP 1506 110, Hahnemühle). Finally, it was dried in ambient air for an entire night.

#### 5.5. Flow Gas-Phase Catalytic Testing

The catalytic tests were performed in a reaction setup consisting of a quartz tube, equipped with an online MS (Gas analysis system, OmniStar, Pfeiffer Vacuum). The reactor was loaded with 20 mg of catalyst, and a pretreatment was performed: the solid was heated to 250 °C with a heating rate of 10 °C/min in 20 vol% synthetic air, with argon being the carrier, at a total flow of 50 mL/min, and this temperature was kept for 30 min. The catalytic tests were performed in 3.8 vol% 2-propanol/3.8 vol% O<sub>2</sub>, oxygen contained in synthetic air, with argon being the carrier. The sample was heated to 400 °C with a heating rate of 2 °C/min, and after 30 min, the sample was cooled to 50 °C with a cooling rate of 2 °C/min. The heating cycle was repeated a second time under the same conditions.

#### Acknowledgments

The authors acknowledge support from the Analytical Instrumentation Center (AIC), the X-ray Center (XRC), and the University Service Facility for Transmission Electron Microscopy (USTEM) at TU Wien. F. Valentini, N. Yigit, G. A. S. Alves, T. Wicht, and B. Wellscheid are also gratefully acknowledged. This research was funded by the Austrian Science Fund (FWF) 10.55776/F8100. For open access purposes, the authors have applied a CC-BY public copyright license to any author accepted manuscript version arising from this submission. The authors acknowledge TU Wien Bibliothek for financial support through its Open Access Funding Programme.

#### Conflict of Interests

The authors declare no conflict of interest.

#### Data Availability Statement

The data that support the findings of this study are available in the Supporting Information of this article.

**Keywords:** Alcohol oxidation · Cobaltite · Flow reaction · Liquid phase · Spinel oxide

- [1] G. D. Yadav, R. K. Mewada, D. P. Wagh, H. G. Manyar, *Catal. Sci. Technol.* **2022**, *12*, 7245–7269.
- [2] G. L. Patrick, *Organic Chemistry*, Taylor & Francis, London **2004**.
- [3] C. Xu, C. Zhang, H. Li, X. Zhao, L. Song, X. Li, *Catal. Surv. Asia* **2016**, *20*, 13–22.
- [4] B.-Z. Zhan, A. Thompson, *Tetrahedron* **2004**, *60*, 2917–2935.
- [5] C. Parmeggiani, F. Cardona, *Green Chem.* **2012**, *14*, 547–564.
- [6] J. V. Ochoa, F. Cavani, in *Gas-Phase Oxidation of Alcohols: Innovation in Industrial Technologies and Recent Developments* (Eds: F. Cardona, C. Parmeggiani), The Royal Society of Chemistry, Cambridge **2014**.
- [7] S. Najafshirtari, K. Friedel Ortega, M. Douthwaite, S. Pattison, G. J. Hutchings, C. J. Bondue, K. Tschulik, D. Waffel, B. Peng, M. Deitermann, G. W. Busser, M. Muhler, M. Behrens, *Chem. Eur. J.* **2021**, *27*, 16809–16833.
- [8] C. Sievers, Y. Noda, L. Qi, E. M. Albuquerque, R. M. Rioux, S. L. Scott, *ACS Catal.* **2016**, *6*, 8286–8307.
- [9] K. Prabu, M. Prabu, A. K. Venugopal, A. T. Venugopalan, W. V. Y. S. Sandilya, C. S. Gopinath, T. Raja, *Appl. Catal., A* **2016**, *525*, 237–246.
- [10] H. Mistry, F. Behafarid, E. Zhou, L. K. Ono, L. Zhang, B. Roldan Cuenya, *ACS Catal.* **2014**, *4*, 109–115.
- [11] T. Yan, J. Gong, C. B. Mullins, *J. Am. Chem. Soc.* **2009**, *131*, 16189–16194.
- [12] G. Mitran, S. Chen, D.-K. Seo, *RSC Adv.* **2020**, *10*, 25125–25135.
- [13] a) S. Mostrou, A. Nagl, M. Ranocchiarri, K. Föttinger, J. A. van Bokhoven, *Chem. Commun.* **2019**, *55*, 11833–11836; b) S. E. Davis, M. S. Ide, R. J. Davis, *Green Chem.* **2013**, *15*, 17–45; c) C. Zhou, Z. Guo, Y. Dai, X. Jia, H. Yu, Y. Yang, *Appl. Catal., B* **2016**, *181*, 118–126; d) X. Dong, Y. Jia, M. Zhang, S. Ji, L. Leng, J. Hugh Horton, C. Xu, C. He, Q. Tan, J. Zhang, Z. Li, *Chem. Eng. J.* **2023**, *451*, 138660; e) E. Aneggi, F. Campagnolo, J. Segato, D. Zuccaccia, W. Baratta, J. Llorca, A. Trovarelli, *Mol. Catal.* **2023**, *540*, 113049; f) H. M. Alshammari, J. R. Humaidi, M. S. Alhumaimess, O. F. Aldosari, M. H. Alotaibi, H. M. A. Hassan, I. Wawata, *React. Kinet., Mech. Catal.* **2019**, *128*, 97–108; g) T. Li, F. Liu, Y. Tang, L. Li, S. Miao, Y. Su, J. Zhang, J. Huang, H. Sun, M. Haruta, A. Wang, B. Qiao, J. Li, T. Zhang, *Angew. Chem., Int. Ed.* **2018**, *57*, 7795–7799.
- [14] K. E. Sickafus, J. M. Wills, N. W. Grimes, *J. Am. Ceram. Soc.* **1999**, *82*, 3279–3292.

- [15] R. J. Hill, J. R. Craig, G. V. Gibbs, *Phys. Chem. Miner.* **1979**, *4*, 317–339.
- [16] a) Y. Li, J. Zhao, J. Jiang, X. He, *Mater. Chem. Phys.* **2003**, *82*, 991–996; b) E. Ríos, S. Abarca, P. Daccarett, H. Nguyen Cong, D. Martel, J. F. Marco, J. R. Gancedo, J. L. Gautier, *Int. J. Hydrogen Energy* **2008**, *33*, 4945–4954.
- [17] a) S. A. Hosseini, M. C. Alvarez-Galvan, J. L. G. Fierro, A. Niaei, D. Salari, *Ceram. Int.* **2013**, *39*, 9253–9261; b) F. Kong, *Electrochim. Acta* **2012**, *68*, 198–201.
- [18] a) Z.-Y. Tian, P. H. Tchoua Ngamou, V. Vannier, K. Kohse-Höinghaus, N. Bahlawane, *Appl. Catal., B* **2012**, *117–118*, 125–134; b) K. Uusi-Esko, E. L. Rautama, M. Laitinen, T. Sajavaara, M. Karppinen, *Chem. Mater.* **2010**, *22*, 6297–6300.
- [19] J. Kaczmarczyk, F. Zasada, J. Janas, P. Indyka, W. Piskorz, A. Kotarba, Z. Sojka, *ACS Catal.* **2016**, *6*, 1235–1246.
- [20] L. Lukashuk, N. Yigit, R. Rameshan, E. Kolar, D. Teschner, M. Hävecker, A. Knop-Gericke, R. Schlögl, K. Föttinger, G. Rupprechter, *ACS Catal.* **2018**, *8*, 8630–8641.
- [21] S. Wang, Z. Ding, X. Wang, *Chem. Commun.* **2015**, *51*, 1517–1519.
- [22] M. G. Walter, E. L. Warren, J. R. McKone, S. W. Boettcher, Q. Mi, E. A. Santori, N. S. Lewis, *Chem. Rev.* **2010**, *110*, 6446–6473.
- [23] Y. Liang, Y. Li, H. Wang, J. Zhou, J. Wang, T. Regier, H. Dai, *Nat. Mater.* **2011**, *10*, 780–786.
- [24] F. Cheng, J. Shen, B. Peng, Y. Pan, Z. Tao, J. Chen, *Nat. Chem.* **2011**, *3*, 79–84.
- [25] P. Liu, H. He, G. Wei, X. Liang, F. Qi, F. Tan, W. Tan, J. Zhu, R. Zhu, *Appl. Catal., B* **2016**, *182*, 476–484.
- [26] J. Chen, W. Shi, S. Yang, H. Arandiyani, J. Li, *J. Phys. Chem. C* **2011**, *115*, 17400–17408.
- [27] S. Periyasamy, P. Subramanian, E. Levi, D. Aurbach, A. Gedanken, A. Schechter, *ACS Appl. Mater. Interfaces* **2016**, *8*, 12176–12185.
- [28] L. Gurrula, A. S. Nagpure, H. R. Gurav, S. Chilukuri, *ChemistrySelect* **2018**, *3*, 3751–3761.
- [29] L. Yao, L. Zhang, Y. Liu, L. Tian, J. Xu, T. Liu, D. Liu, C. Wang, *CrystEngComm* **2016**, *18*, 8887–8897.
- [30] T. Falk, E. Budiyanto, M. Dreyer, C. Pflieger, D. Waffel, J. Büker, C. Weidenthaler, K. F. Ortega, M. Behrens, H. Tüysüz, M. Muhler, B. Peng, *ChemCatChem* **2021**, *13*, 2942–2951.
- [31] T. Falk, E. Budiyanto, M. Dreyer, J. Büker, C. Weidenthaler, M. Behrens, H. Tüysüz, M. Muhler, B. Peng, *ACS Appl. Nano Mater.* **2022**, *5*, 17783–17794.
- [32] S. Mostrou, T. Sipócz, A. Nagl, B. Földi, F. Darvas, K. Föttinger, J. A. van Bokhoven, *React. Chem. Eng.* **2018**, *3*, 781–789.
- [33] R. Ciriminna, V. Pandarus, F. Béland, Y.-J. Xu, M. Pagliaro, *Org. Process Res. Dev.* **2015**, *19*, 1554–1558.
- [34] X. Liu, C. Prewitt, *Phys. Chem. Miner.* **1990**, *17*, 168–172.
- [35] V. Bartůněk, Š. Huber, D. Sedmidubský, Z. Sofer, P. Šimek, O. Jankovský, *Ceram. Int.* **2014**, *40*, 12591–12595.
- [36] S. Liu, D. Ni, H.-F. Li, K. N. Hui, C.-Y. Ouyang, S. C. Jun, *J. Mater. Chem. A* **2018**, *6*, 10674–10685.
- [37] H. Bordeneuve, S. Guillemet-Fritsch, A. Rousset, S. Schuurman, V. Poulain, *J. Solid State Chem.* **2009**, *182*, 396–401.
- [38] L. Han, Q. Meng, D. Wang, Y. Zhu, J. Wang, X. Du, E. A. Stach, H. L. Xin, *Nat. Commun.* **2016**, *7*, 13335.
- [39] N. H. Perry, T. O. Mason, *J. Am. Ceram. Soc.* **2013**, *96*, 966–971.
- [40] M. Peiteado, A. C. Caballero, D. Makovec, *J. Ceram. Soc. Jpn.* **2010**, *118*, 337–340.
- [41] L. André, S. Abanades, L. Cassayre, *J. Solid State Chem.* **2017**, *253*, 6–14.
- [42] M. Thommes, K. Kaneko, A. V. Neimark, J. P. Olivier, F. Rodriguez-Reinoso, J. Rouquerol, K. S. W. Sing, *Pure Appl. Chem.* **2015**, *87*, 1051–1069.
- [43] R. A. E. Acedera, G. Gupta, M. Mamlouk, M. D. L. Balela, *J. Alloys Compd.* **2020**, *836*, 154919.
- [44] Y. Yang, J. Zhang, L. Xu, P. Li, Y. Liu, W. Dang, *ACS Omega* **2022**, *7*, 9229–9243.
- [45] M. C. Biesinger, B. P. Payne, A. P. Grosvenor, L. W. M. Lau, A. R. Gerson, R. S. C. Smart, *Appl. Surf. Sci.* **2011**, *257*, 2717–2730.
- [46] T. Fernandes, R. R. Mohan, L. Donk, W. Chen, C. Biz, M. Fianchini, S. Kamali, S. M. Alizadeh, A. Kitayev, A. Ashdot, M. Page, L. M. Salonen, S. Kopp, E. T. Gutelmacher, J. Gracia, M. C. Figueiredo, Y. V. Kolen'ko, *Energy Adv.* **2024**, *3*, 2575–2586.
- [47] X. Cai, W. Sun, C. Xu, L. Cao, J. Yang, *Environ. Sci. Pollut. Res.* **2016**, *23*, 18609–18620.
- [48] J. Wang, T. Ye, Y. Shao, Z. Lu, Y. Lin, H. Wu, G. Li, K. Chen, D. Tang, *J. Electrochem. Soc.* **2021**, *168*, 120553.
- [49] W. Wang, L. Kuai, W. Cao, M. Huttula, S. Ollikkala, T. Ahopelto, A.-P. Honkanen, S. Huotari, M. Yu, B. Geng, *Angew. Chem., Int. Ed.* **2017**, *56*, 14977–14981.
- [50] C.-W. Tang, C.-B. Wang, S.-H. Chien, *Thermochim. Acta* **2008**, *473*, 68–73.

Manuscript received: April 29, 2025

Revised manuscript received: July 10, 2025

Accepted manuscript online: July 12, 2025

Version of record online: August 15, 2025